RSC Advances

PAPER

View Article Online
View Journal | View Issue

Cite this: *RSC Adv.*, 2024, **14**, 28320

Enhancing Cr(VI) removal performance of $Ti_3C_2T_x$ through structural modification by using a spray freezing method

Linjie Yi,†[a] Hongwei Wang,†[a] Xianliang Ren,[a] GaoBin Liu,[a] Hongen Nian,[c] Zhiqin Zheng*[def] and Fang Wu *[ab]

Structural modification is expected to be a facile way to enhance the adsorption performance of MXene. In this work, the structural modification of $Ti_3C_2T_x$ was carried out by a spray freezing method, and two kinds of nano-structure (spherical and flaky) of $Ti_3C_2T_x$ were prepared by adjusting the solution concentration of $Ti_3C_2T_x$. Then the Cr(VI) adsorption capacity and removal efficiency of the spherical and flaky $Ti_3C_2T_x$ was investigated, respectively. It is found that flaky $Ti_3C_2T_x$ was produced with a $Ti_3C_2T_x$ concentration of 3 mg mL^{-1}, while spherical $Ti_3C_2T_x$ was obtained with a concentration of 6 mg mL^{-1}. The long diameter of flaky $Ti_3C_2T_x$ is about 8–10 μm, and the specific surface area is 17.81 m^2 g^{-1}. While spherical $Ti_3C_2T_x$ had a diameter of about 1–4 μm and a specific surface area of 17.07 m^2 g^{-1}. The optimized structure of flaky and spherical $Ti_3C_2T_x$ improves the maximum adsorption capacity by 97% and 33%, respectively, compared with the few-layer $Ti_3C_2T_x$. The maximum adsorption capacity of flaky $Ti_3C_2T_x$ was 928 mg g^{-1}, while that of spherical $Ti_3C_2T_x$ was 626 mg g^{-1}. The adsorption capacity of both $Ti_3C_2T_x$ structures decreased with the increase of pH, and reached the maximum value at pH = 2; meanwhile, the adsorption capacity of both $Ti_3C_2T_x$ structures increased with the increase of Cr(VI) concentration. The adsorption of Cr(VI) on flaky $Ti_3C_2T_x$ was very fast, reaching equilibrium in 3 min, while spherical $Ti_3C_2T_x$ took 5 min. The adsorption of Cr(VI) on both $Ti_3C_2T_x$ structures belonged to the monolayers, heat-absorbing chemical adsorption, and the diffusion process of Cr(VI) was regulated by the external diffusion and internal diffusion of particles. Its adsorption mechanism was the combination of reductive adsorption and electrostatic adsorption.

Received 25th June 2024
Accepted 16th August 2024

DOI: 10.1039/d4ra04640d

rsc.li/rsc-advances

1. Introduction

Heavy metal ions pose a great threat to human health because of their toxicity and high migration and enrichment in living organisms.[1] With the rapid advancement in metallurgy, electroplating, and tanning, a large amount of wastewater containing Cr(VI) has been produced.[2] Cr(VI) is not only toxic and carcinogenic, but it also causes a variety of health problems, including liver damage,[3] vomiting,[4] and lung congestion.[5] Therefore, effective removal of Cr(VI) from water is essential. In modern industry, the standard treatment method for wastewater containing Cr(VI) consists of two steps: reducing Cr(VI) to Cr(III) using a chemical agent such as sodium bisulfite or sulfur dioxide gas, and then adjusting the pH to promote the precipitation of Cr(III).[6] However, the process is complex and requires the use of large amounts of acids and bases, which can lead to serious secondary wastewater problems. In addition, other treatment methods have also been widely reported, such as electrolysis,[7] ion exchange,[8] membrane separation,[9] chemical precipitation,[10] adsorption,[11] photocatalysis,[12] *etc.*, among which the adsorption method has attracted much attention due to its low cost and simplicity of operation.

The selection of adsorbent is key to the removal of heavy metal ions by adsorption. Compared with other adsorbent materials, two-dimensional materials have the advantages of large specific surface area and abundant active centers, and are ideal adsorbents.[13] Typical 2D carbon nanomaterials such as

[a]*Chongqing Key Laboratory of Interface Physics in Energy Conversion, College of Physics, Chongqing University, Chongqing, 400044, P. R. China. E-mail: wufang@cqu.edu.cn*

[b]*Center of Modern Physics, Institute for Smart City of Chongqing University in Liyang, Liyang, Jiangsu Province, 213300, P. R. China*

[c]*Qinghai Institute of Salt Lakes, Key Laboratory of Green and High-end Utilization of Salt Lake Resources, Chinese Academy of Sciences, Xining, Qinghai Province, 810008, P. R. China*

[d]*Sichuan Province Engineering Technology Research Center of Liquor-Making Grains, School of Biological Engineering and Wuliangye Liquor, Sichuan University of Science and Engineering, Yibin, Sichuan Province, 644000, China. E-mail: zhengzhiqin168@163.com*

[e]*National Innovation Center for Nuclear Enviromental Safety, Southwest University of Science and Technology, Mianyang, Sichuan Province, 621010, P. R. China*

[f]*NHC Key Laboratory of Nuclear Technology Medical Transformation (MianYang Central Hospital), Mianyang, Sichuan Province, 621010, P. R. China*

† These authors contributed to the work equally and should be regarded as co-first authors.

graphene,[14] graphene oxide[15] and their derivatives[16] show excellent properties in ion adsorption and organic pollution treatment. However, the disadvantages such as high cost and single surface functional groups greatly limit their practical application.[17] MXene is a novel two-dimensional material composed of transition metal carbides or nitride, which has many similar properties to graphene. Simultaneously, it has the advantages of large layer spacing, abundant surface functional groups, large specific surface area, strong affinity with metal ions, and good hydrophilicity, *etc.*,[18] which shows unique advantages in the treatment of heavy metal ion wastewater by photocatalysis[19] and adsorption. It is considered to be an ideal material for removing heavy metal ions.

$Ti_3C_2T_x$ is the earliest MXenes material prepared due to its relatively simple preparation method, stable mechanical properties and excellent physical and chemical properties, $Ti_3C_2T_x$ has become a widely studied and applied material. $Ti_3C_2T_x$ and its composites demonstrated excellent adsorption properties on Cr(VI) treatment. In 2018, Tang *et al.* prepared organ-like multilayer $Ti_3C_2T_x$ solution by HF etching, with a maximum adsorption capacity (MAC) of 80 mg g^{-1} for Cr(VI).[20] In 2019, He *et al.* prepared $Ti_3C_2T_x$ with zero-valent iron intercalation nanoparticles, its MAC for Cr(VI) is 194.87 mg g^{-1}.[21] The MAC of $Ti_3C_2T_x$ for Cr(VI) obtained using trifluoroacetic acid (TFA) etching by Zhu *et al.* in 2022 was 351 mg g^{-1}.[22] Howerver, despite exhibiting remarkable adsorption capabilities for heavy metal ions, MXene is not immune to the inherent self-stacking problem of two-dimensional materials.[23] This self-stacking significantly reduces the accessible specific surface area of MXene, thereby limiting its adsorption capacity.[24]

To solve the problem of self-stacking in MXene, a common approach involves the introduction of interlayer "pillars" such as polymers,[25] nanoparticles,[26] nanotubes,[27] and nanosheets.[28] These pillars ensure adequate spacing between the layers. Gogotsi and colleagues also proposed a templatie method to build three-dimensional structures from 2D materials to synthesize MXene with a large specific surface area.[29] However, these methods are highly complex. Therefore, it is highly necessary to explore simple and efficient methods to prevent the self-stacking.

In our previous work, the heavy metal ion Cr(VI) have been tried to be removed by 2D material, such as LDH[30] or $Ti_3C_2T_x$ (ref. 4) or Ti_2CT_x (ref. 31) and we found that the Cr(VI) adsorption capacity can be further enhanced by adjusting the functional groups or modifying the structure of $Ti_3C_2T_x$.

In this paper, a simple spray freezing technique has been used to prepare spherical and flaky structures of $Ti_3C_2T_x$, both of which effectively increase the specific surface area. The adsorption performance of these two structures was investigated, and the adsorption process of Cr(VI) on $Ti_3C_2T_x$ was analyzed using adsorption kinetic models, isotherm models, and intraparticle diffusion models. Additionally, the effects of temperature, pH and other parameters on the adsorption characteristics were also discussed. The changes of binding energy before and after adsorption were also analyzed using XPS, shedding light on the adsorption mechanism.

2. Experimental methods

2.1 Chemicals

The raw materials for this study are used directly after purchase without further treatment. Ti_3AlC_2 (>98 wt%, 200 mods) was bought from Fussman, lithium fluoride (LiF, 99%), hydrochloric acid (HCl, 9 M), sodium hydroxide (NaOH, 5 M), nitric acid (HNO_3, 70%) and potassium dichromate ($K_2Cr_2O_7$, 99.9%) from Shanghai Aladdin Co., LTD.

2.2 Preparation of few-layer $Ti_3C_2T_x$

The few-layer of $Ti_3C_2T_x$ were obtained by etching the precursor Ti_3AlC_2 with a mixture of HCl and LiF. Ti_3AlC_2 : HCl : LiF was mixed according to the ratio of 1 g : 20 mL : 1.6 g, stirred magnetically at 50 °C with 1000 rpm for 24 h, and then the mixture was washed and centrifuged multiple times with deionized (DI) water until the pH of solution reached 6. After ultrasonic treatment for 3 h, the upper layer solution was collected by further centrifugation at 3500 rpm for 30 min. The collected solution turned green after dilution and formed a stable and uniform suspension, indicating successful preparation of $Ti_3C_2T_x$ with few layers. A solution sample (20 mL) was filtered, dried, and weighed to determine a concentration of 6 mg mL^{-1} before being stored in the refrigerator.

2.3 Preparation of spherical and flaky $Ti_3C_2T_x$

1 L of liquid nitrogen was added to the beaker, and few-layer $Ti_3C_2T_x$ with a density of 6 mg mL^{-1} was sprayed evenly into the liquid nitrogen using a sprayer. The ejected droplet was instantly frozen into a ball in the liquid nitrogen at −160 °C, and the two-dimensional $Ti_3C_2T_x$ sheet was also frozen into a $Ti_3C_2T_x$ ball under the action of the droplet freezing stress. The preparation process of flaky $Ti_3C_2T_x$ is similar to that of spherical $Ti_3C_2T_x$, except that the concentration of few-layer $Ti_3C_2T_x$ changes from 6 mg mL^{-1} to 3 mg mL^{-1}. The preparation process is shown in the Fig. 1.

2.4 Characterization

The crystal structure of the samples was analyzed by an X-ray diffractometer (XRD, X'Pert Powder X, PANalytical) with the testing angles of 5–80° and a scanning speed of 2° min^{-1}, the morphology was examined by an scanning electron microscope (SEM, JSM-6800F, JEOL), the surface charge was assessed by the zeta potential analyzer (NanoBrook Omni, Brookhaven), the binding energy and valence change were measured by an X-ray photoelectron spectroscope (XPS, ESCALAB 250Xi, Thermo Fisher Scientific), the nitrogen adsorption and desorption isotherms were determined with a fully automatic multi-station specific surface and aperture analyzer (BELSORP-max II), and the concentration of Cr(VI) solution was determined by a UV-vis spectrophotometer (UV-3600, Shimadzu).

2.5 Cr(VI) adsorption experiments

The $K_2Cr_2O_7$ powder was dissolved in DI water to obtain Cr(VI) solutions with different concentrations. During the adsorption

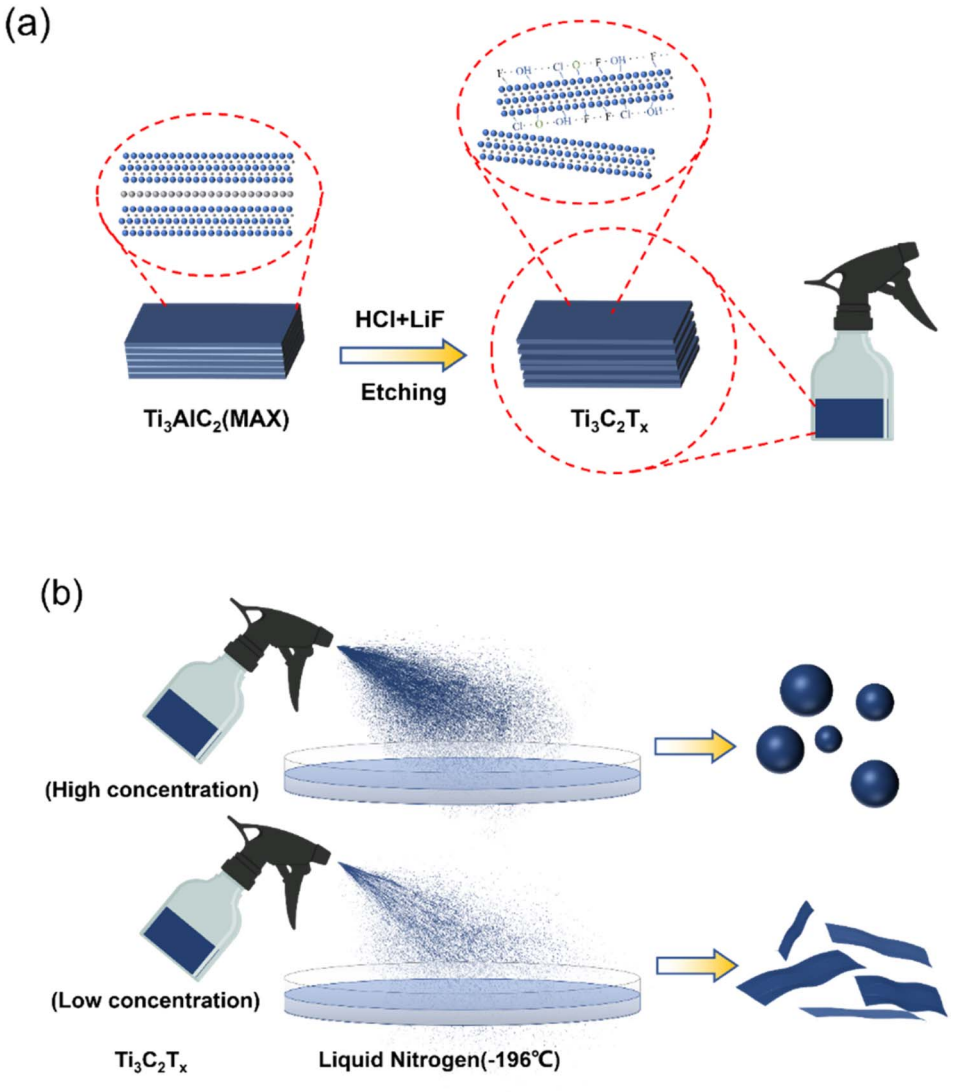

Fig. 1 (a) Preparation process of the few-layer $Ti_3C_2T_x$; (b) preparation of the flaky and spherical $Ti_3C_2T_x$ by spray freezing method.

Table 1 Experimental parameters for Cr(VI) adsorption by $Ti_3C_2T_x$

Category	pH	Adsorption time (min)	Adsorbent concentration (mg L^{-1})	Temperature (K)
pH	1/2/4/6/8	60	120	298
Adsorption time	2	0.5/1/2/5/10/20/30/60	150/200/250; 175/250/300	298
Adsorbent concentration	2	60	100/125/150/175/200/225/250/275	298
Temperature	2	60	200	298/313/328

process, 100 mL of $K_2Cr_2O_7$ solution was used and the pH of the solution was pre-adjusted with nitric acid or sodium hydroxide. Except for the pH effect study, the pH value of other adsorption experiments was maintained at 2. The mass of $Ti_3C_2T_x$ used in all experiments was 20 mg. The prepared adsorbent solution was dropped into the $K_2Cr_2O_7$ solution at a magnetic stirring rate of 600 rpm. The experimental temperature was maintained at 25 °C. After different adsorption time, the middle part of the mixed solution was extracted and filtered to test the concentration of residual Cr(VI) in the solution. The adsorption capacity q_e (mg g^{-1}) and removal rate R (%) at different times were calculated using the equations as follows (1)–(3):[32]

$$q_t = \frac{(C_0 - C_t)V}{m} \quad (1)$$

$$q_e = \frac{(C_0 - C_e)V}{m} \quad (2)$$

$$R\% = \frac{C_0 - C_e}{C_0} \quad (3)$$

where q_t (mg g^{-1}) is the adsorption capacity at time t, q_e (mg g^{-1}) is the adsorption capacity at equilibrium moment, R is the removal efficiency, C_0 (mg g^{-1}) is the initial concentration of the solution, C_t (mg g^{-1}) is the solution concentration at time t, C_e (mg g^{-1}) is the concentration of the solution at equilibrium moment, V (L) is the volume of the solution, m (g) is the mass of the adsorbent used. The specific experimental parameters of this work are shown in the Table 1.

3. Results and discussion

3.1 Structure and morphology characterization

The XRD patterns of precursor Ti_3AlC_2, few layer, flaky and spherical $Ti_3C_2T_x$ are shown in Fig. 2(a). It is found that before etching, the diffraction peaks of the precursor Ti_3AlC_2 were distributed in 9.5° (002), 34° (100), 38.8° (006) and 52.3° (106). After 24 h of etching, the diffraction peak of (002) moved to a smaller angle, from 9.5° to 7.6°, and the remaining diffraction peaks disappeared. It can be proved that the Al layer were completely etched away. After spray freezing in liquid nitrogen, compared with that of few-layer $Ti_3C_2T_x$, the (002) diffraction peak of the prepared spherical $Ti_3C_2T_x$ continues to move to a smaller angle, (6.3°). The prepared flaky $Ti_3C_2T_x$ has the smallest (002) diffraction peak with an angle of 5.5°. The shift of the diffraction peak to a smaller angle indicates that the lattice spacing of the sample increases after liquid nitrogen spray freezing.

The N_2 adsorption–desorption isotherms of few-layer $Ti_3C_2T_x$, spherical $Ti_3C_2T_x$ and flaky $Ti_3C_2T_x$ are given in Fig. 2(b). The specific surface area of few-layer $Ti_3C_2T_x$, spherical $Ti_3C_2T_x$ and flaky $Ti_3C_2T_x$ is 6.05 m^2 g^{-1}, 17.07 m^2 g^{-1} and 17.81 m^2 g^{-1}, respectively. The results show that the specific surface area of spheroidal $Ti_3C_2T_x$ and flaky $Ti_3C_2T_x$ increased by 1.82 times and 1.94 times, respectively, compared with few-layer $Ti_3C_2T_x$ after spray freezing. A larger specific surface area means that more active sites can be exposed, which is more conducive to adsorption.

The morphology and microstructure of the samples were characterized by scanning electron microscopy (SEM). As displayed in Fig. 3(a), the precursor Ti_3AlC_2 is a tightly packed massive structure. Fig. 3(b) shows that after etching, few-layer $Ti_3C_2T_x$ with an average diameter of about 16 μm is obtained. Then few-layer $Ti_3C_2T_x$ was spray frozen in liquid nitrogen with differnet $Ti_3C_2T_x$ concentrations and freeze-dried at low temperature. Fig. 3(c) shows that spherical $Ti_3C_2T_x$ was successfully prepared by spray freezing technology with a $Ti_3C_2T_x$ concentration of 6 mg mL^{-1}. After spray freezing, $Ti_3C_2T_x$ basically formed a very regular round sphere with a diameter of 1–4 μm, and the sheet structure was almost invisible. Fig. 3(d) exhibits that the surface of the sphere is as smooth as that of $Ti_3C_2T_x$. Because the spray is not uniform, the size of the prepared sphere is also not uniform. Fig. 3(e) shows that flaky $Ti_3C_2T_x$ with better dispersion was successfully prepared with low concentration (3 mg mL^{-1}) $Ti_3C_2T_x$ spray. From Fig. 3(f) it can be seen that the flaky $Ti_3C_2T_x$ of 3 × 3 μm distribute in a gauzy manner, and the dispersion of the flaky $Ti_3C_2T_x$ after spray freezing is significantly higher than that of the few-layer $Ti_3C_2T_x$. It indicates that the low concentration of $Ti_3C_2T_x$ dispersion can effectively disperse $Ti_3C_2T_x$ by spray freezing treatment and prevent the stacking of $Ti_3C_2T_x$.

3.2 Adsorption capacity

The time dependent adsorption performance of the spherical and flaky $Ti_3C_2T_x$ are exhibited in Fig. 4(a) and (b), respectively. It can be seen that the spherical and flaky $Ti_3C_2T_x$ solution reached the adsorption equilibrium at about 5 min and 3 min respectively. In order to discuss the effect of $Ti_3C_2T_x$ structures on the adsorption performance of Cr(VI), The adsorption properties of 20 mg untreated few layer, spherical and flaky $Ti_3C_2T_x$ for 100 mL Cr(VI) solution at 250 mg L^{-1} were studied. The adsorption capacity at equilibrium was compared and shown in Fig. 4(c). It is found that the MAC of 20 mg few-layer, spherical and flaky $Ti_3C_2T_x$ at equilibrium reached 472, 626 and 928 mg g^{-1}, respectively, means that the adsorption capacity of spherical and flaky $Ti_3C_2T_x$ was 33% and 97% larger than that of few-layer $Ti_3C_2T_x$, respectively. The reason for this phenomenon is

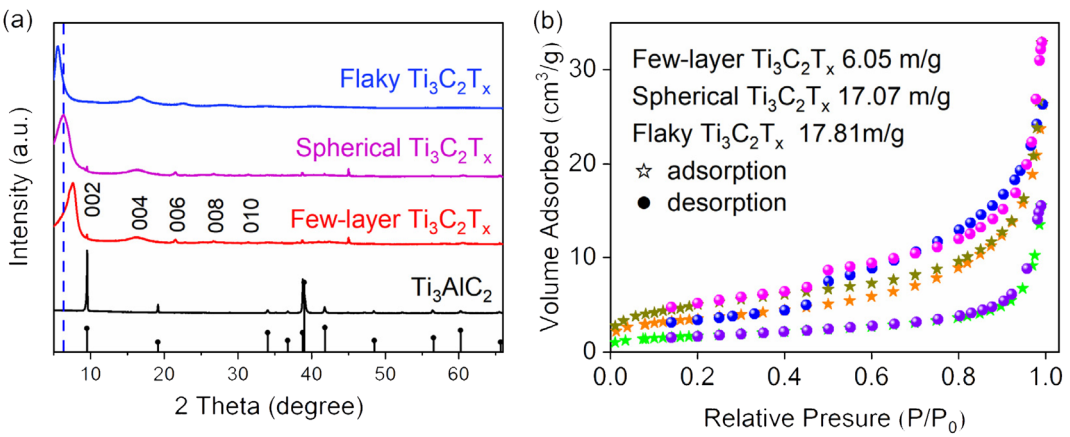

Fig. 2 (a) XRD patterns of precursor Ti_3AlC_2, few-layer $Ti_3C_2T_x$, spherical and flaky $Ti_3C_2T_x$; (b) N_2 adsorption–desorption isotherm diagram of the few-layer $Ti_3C_2T_x$, spherical $Ti_3C_2T_x$ and flaky $Ti_3C_2T_x$.

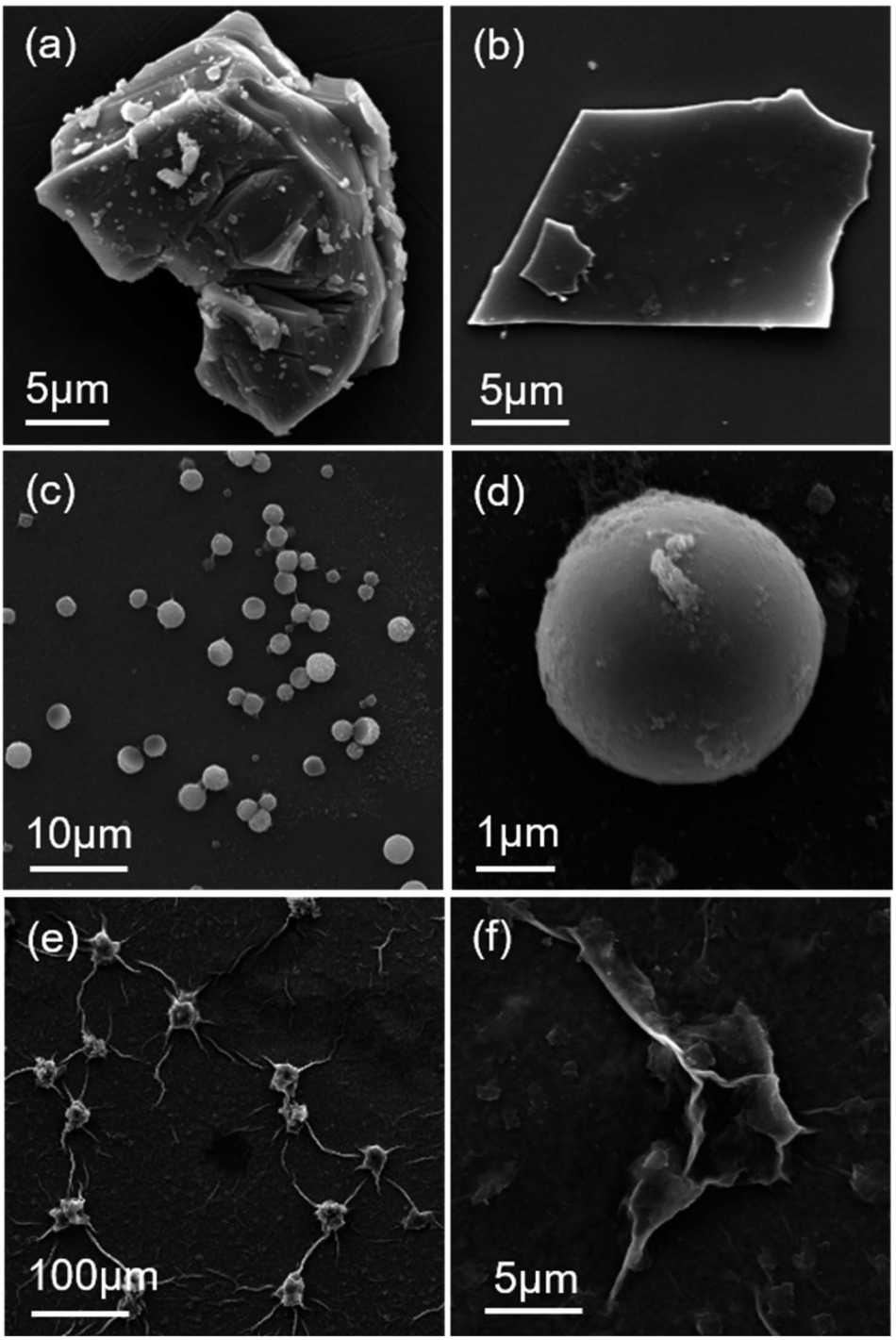

Fig. 3 SEM images of (a) precursor Ti_3AlC_2, (b) few-layer $Ti_3C_2T_x$, (c and d) spherical $Ti_3C_2T_x$, and (e and f) flaky $Ti_3C_2T_x$.

that the specific surface area of flaky $Ti_3C_2T_x$ is larger than that of spherical structures, and the flaky ones are more dispersed.

3.3 Adsorption kinetics

The pseudo-first-order kinetic model[33] is as follows:

$$\lg(q_e - q_t) = \lg q_e - \frac{k_1}{2.303} \times t \quad (4)$$

The pseudo-second-order kinetic model[34] is:

$$\frac{t}{q_t} = \frac{1}{k_2 q_e^2} + \frac{t}{q_e} \quad (5)$$

The in-particle diffusion model[35] is:

$$q_t = k_i t^{\frac{1}{2}} + C_i \quad (6)$$

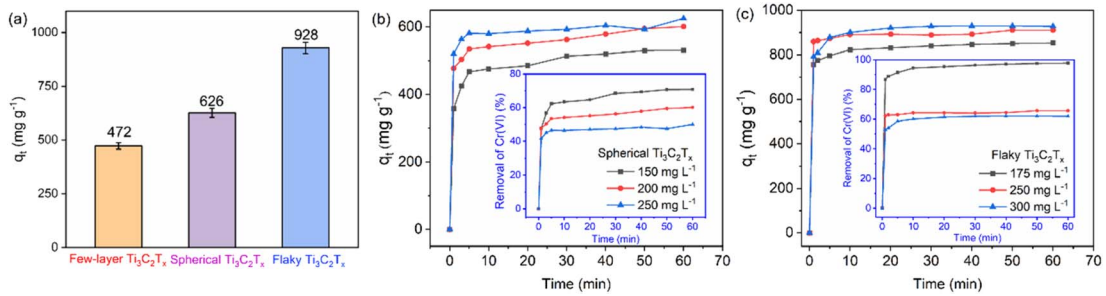

Fig. 4 (a) The change of adsorption capacity and removal rate of spherical $Ti_3C_2T_x$ with time; (b) the change of adsorption capacity and removal rate of flaky $Ti_3C_2T_x$ with time; (c) comparison diagram of Cr(VI) maximum adsorption capacity of the few-layer $Ti_3C_2T_x$, the spherical $Ti_3C_2T_x$ and the flaky $Ti_3C_2T_x$.

where k_1 and k_2 are the constants of the corresponding kinetic model respectively, and k_i is the coefficient of stage i in the intra-particle diffusion model. In this study, 20 mg spherical $Ti_3C_2T_x$ and flaky $Ti_3C_2T_x$ were used as adsorbents, and the adsorption results of Cr(VI) at different initial concentrations were fitted according to the above three models. As shown in Fig. 5a and b, the fitting results show that the correlation coefficients of the pseudo-second-order kinetic model for Cr(VI) adsorption by spherical and flaky $Ti_3C_2T_x$ are closer to 1. By comparing the fitted parameters of kinetic model in Table 2, the theoretical equilibrium adsorption capacity calculated by pseudo-second-order kinetic model is closer to the experimental results. Therefore, the pseudo-second-order kinetic model is more consistent with the adsorption process of Cr(VI) by the spherical and flaky $Ti_3C_2T_x$. The pseudo-second-order kinetic model indicates that the adsorption rate is controlled by the bonding rate of the chemical bond between the adsorbent and the adsorbed object, which also indicates that the adsorption of Cr(VI) by the spherical and flaky $Ti_3C_2T_x$ belongs to chemical adsorption.

The intraparticle diffusion model holds that adsorption is a complex multi-stage process, namely external diffusion, in-particle diffusion, and adsorption at the adsorption site within the adsorbents. As shown in Fig. 5(e), the first stage of the adsorption of Cr(VI) by spherical $Ti_3C_2T_x$ occurred within 10 min after the adsorption began. At this stage, Cr(VI) rapidly diffuse to the outer surface of $Ti_3C_2T_x$, and the adsorption reaction occurs on the outer surface. 10 to 30 min is the second stage of adsorption. With the progress of adsorption, the adsorption on the outer surface of $Ti_3C_2T_x$ reaches saturation, Cr(VI) enters the $Ti_3C_2T_x$ sphere, and the particles are diffused and adsorbed in the layer. After 30 min, the third stage of diffusion, adsorption and desorption reach dynamic equilibrium, the adsorption amount no longer increases. Fig. 5(f) shows the diffusion model of $Ti_3C_2T_x$ on Cr(VI) particles. The three stages occurred within 2 min, 2 to 10 min and 10 min after the adsorption began. The fitting lines of the intragranular diffusion models of both spheres and $Ti_3C_2T_x$ do not intersect with the origin, indicating that both of them are the internal and external diffusion that jointly governs the adsorption process.

3.4 Adsorption isotherm

The adsorption properties were closely related to the concentration of the adsorbent. In order to analyze the interaction between the adsorbent and Cr(VI), this study tested the MAC after 20 mg $Ti_3C_2T_x$ adsorbed 100 mL Cr(VI) with different concentrations at 308 K and pH 2. As shown in (Fig. 6), with the increase of the initial concentration of Cr(VI), the MAC of spherical and flaky $Ti_3C_2T_x$ at equilibrium also increases gradually. When the initial concentration of Cr(VI) was 300 mg L^{-1}, the MAC of spherical and flaky $Ti_3C_2T_x$ at equilibrium reached 629 and 928 mg g^{-1}, respectively, and the removal efficiency was reduced to 64% and 62%, respectively. In order to analyze the adsorption mechanism, the single layer isothermal adsorption Langmuir model and the Freundlich isotherm model based on isomeric surface adsorption were established. The adsorption data were fitted with two models respectively to find the best. The linear equation of the Langmuir isotherm model[36] is:

$$\frac{C_e}{q_e} = \frac{1}{K_l q_m} + \frac{C_e}{q_m} \quad (7)$$

The linear equation of the Freundlich isotherm model[37] is:

$$\ln q_e = \ln K_F + \frac{1}{n} \ln C_e \quad (8)$$

where C_e (mg L^{-1}) is the concentration of adsorbent at equilibrium, q_e (mg g^{-1}) is the adsorption capacity of adsorbent at equilibrium time of a certain concentration, q_m (mg g^{-1}) is the theoretical maximum adsorption capacity in Langmuir model, and n represents the adsorption strength of Freundlich model. K_L and K_F are the equilibrium adsorption constants of the two models respectively. The Langmuir isotherm models of spherical and flaky $Ti_3C_2T_x$ are more consistent with the experimental data, indicating that the adsorption of Cr(VI) by spherical and flaky $Ti_3C_2T_x$ is monolayer adsorption.

3.5 Adsorption thermodynamics

For 100 mL Cr(VI) at a concentration of 250 mg L^{-1}, MAC of 20 mg spherical and flaky $Ti_3C_2T_x$ solutions with adsorption temperature is shown in Fig. 7(a) The MAC increases with the increase of temperature, indicating that the adsorption process

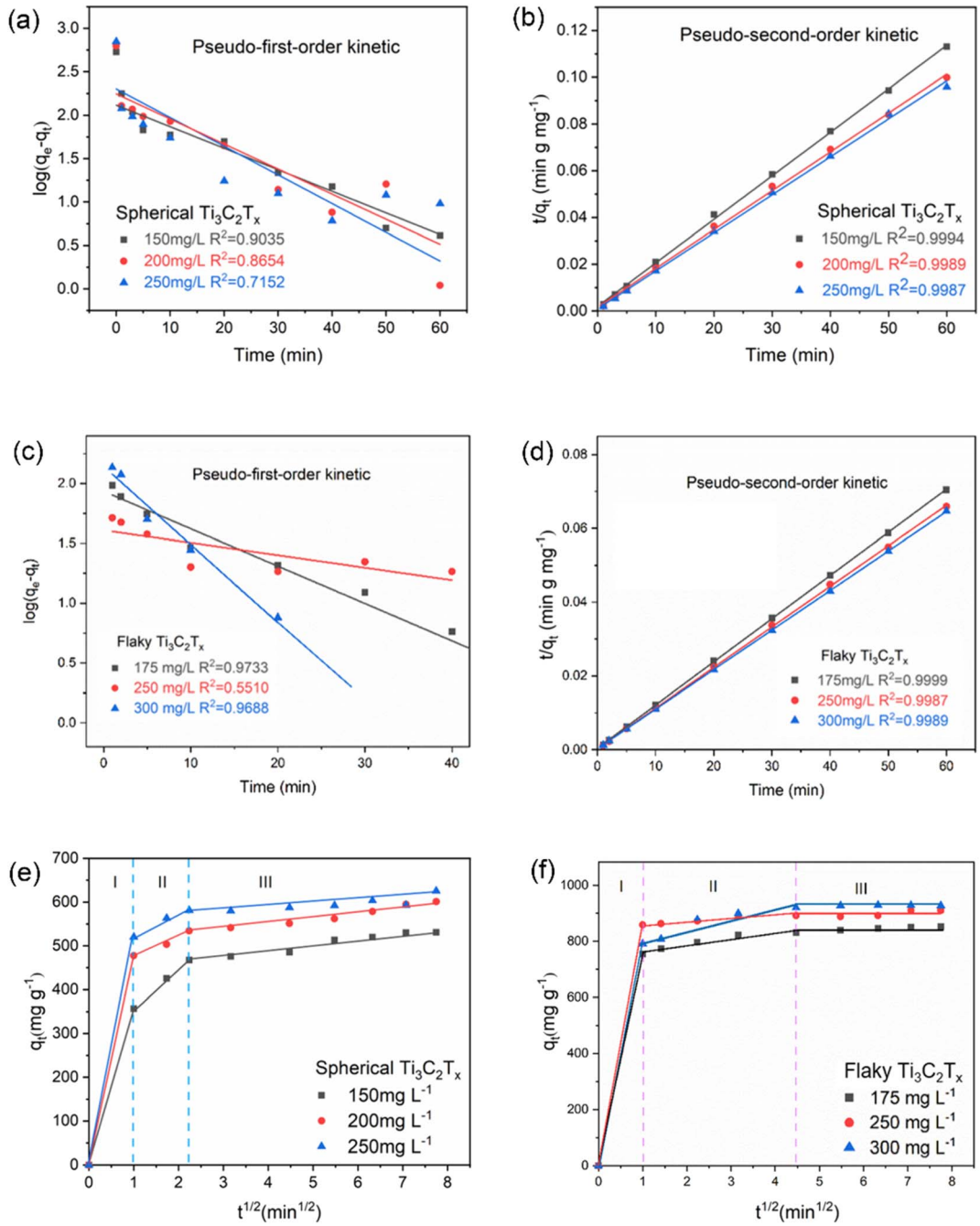

Fig. 5 (a–d) Kinetic models of spherical $Ti_3C_2T_x$ and flaky $Ti_3C_2T_x$; (e and f) Weber–Morris intraparticle diffusion model of spherical $Ti_3C_2T_x$ and flaky $Ti_3C_2T_x$.

is endothermic. The thermodynamic parameters include enthalpy change (ΔH, kJ mol^{-1}) and entropy change (ΔS, J mol^{-1} K^{-1}) were calculated by Van't Hoff equation:[38]

$$K_d = \frac{(C_0 - C_e)V}{mC_e} \quad (9)$$

$$\ln K_d = \frac{\Delta S}{R} - \frac{\Delta H}{RT} \quad (10)$$

Gibbs free energy change (ΔG, kJ mol^{-1}) was calculated from the following equation:

$$\Delta G = \Delta H - T \times \Delta S \quad (11)$$

where K_d is the distribution coefficient (mL g^{-1}), T stands for absolute temperature (K), and R is the ideal gas constant (8.314 J (mol K)$^{-1}$). The linear fitting relationship between ln K_d and $1/T$ is shown in Fig. 7(b), and the relevant parameters are list in Table 3. ΔH is greater than zero, which proves that the

Table 2 Fitting results of pseudo-first-order kinetics and pseudo-second-order kinetics

			Pseudo-first-order model			Pseudo-second-order model		
	C_0 (mg L^{-1})	$q_{e\ exp.}$ (mg g^{-1})	$q_{e\ cal.}$ (mg g^{-1})	k_1	R^2	$q_{e\ cal.}$ (mg g^{-1})	k_2	R^2
S–$Ti_3C_2T_x$	100	535	131	0.057	0.90	538	0.0018	0.99
	125	626	177	0.067	0.86	602	0.0017	0.99
	175	705	202	0.076	0.71	613	0.0030	0.99
F–$Ti_3C_2T_x$	175	804	81	0.054	0.97	850	0.0012	0.99
	250	884	177	0.102	0.55	863	0.0012	0.99
	300	928	253	0.156	0.96	899	0.0011	0.99

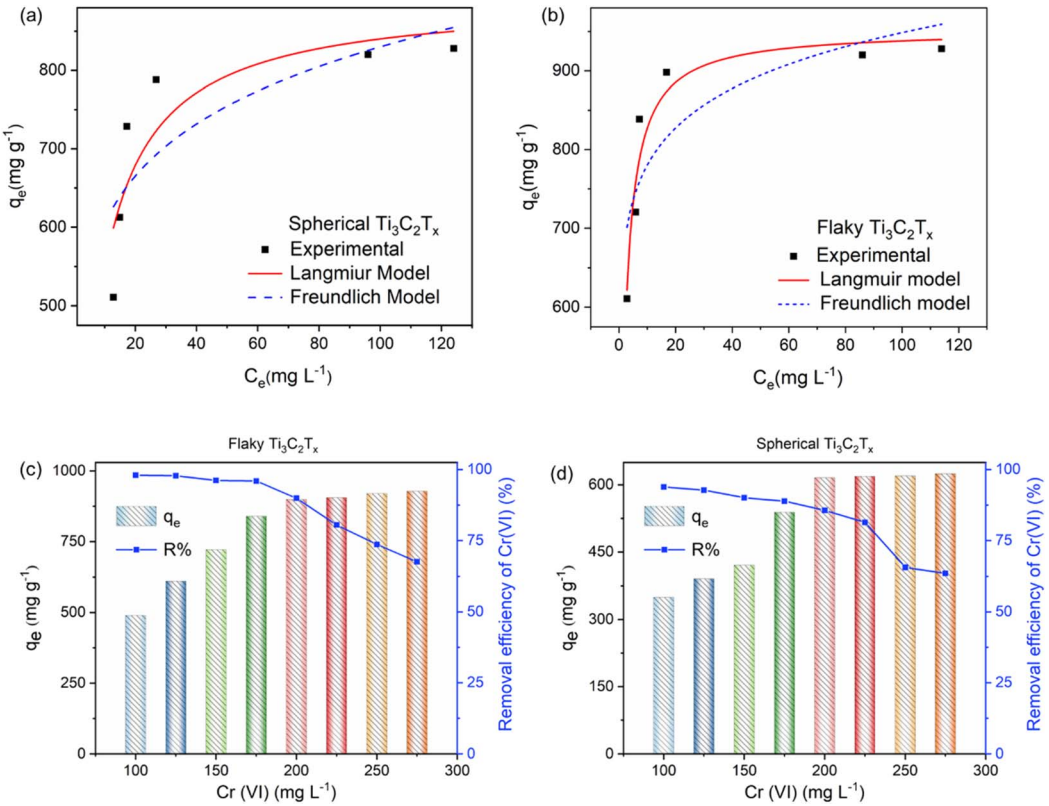

Fig. 6 Langmuir and Freundlich isotherm models of (a) spherical $Ti_3C_2T_x$ and (b) flaky $Ti_3C_2T_x$; (c and d) The removal efficiency and maximum adsorption capacity of spherical $Ti_3C_2T_x$ and flaky $Ti_3C_2T_x$ as a function of Cr(VI) concentration.

adsorption process is endothermic. Positive entropy indicates that randomness between interfaces increases during adsorption. Negative ΔG indicates that the adsorption of Cr(VI) by spheres and $Ti_3C_2T_x$ is a spontaneous chemical reaction process.

3.6 Effect of pH

Adsorption tests were carried out on 100 mL, 300 mg L^{-1} Cr(VI) solution with 20 mg spherical and flaky $Ti_3C_2T_x$ at 308 K, and the effect of different pH on the adsorption of Cr(VI) solution was investigated. The pH value of the solution has a great influence on the existence mode of Cr(VI) and the protonation/deprotonation of $Ti_3C_2T_x$. As shown in Fig. 8(a), the adsorption process of Cr(VI) by spherical and flaky $Ti_3C_2T_x$ solutions is highly dependent on pH value. The adsorption ability of the adsorbent for Cr(VI) is very strong at low pH, and the adsorption capacity decreases rapidly with the increase of pH value. The result may be attributed to the fact that the presence of Cr(VI) varies with different pH, and potassium dichromate is a strong oxidizing agent in low pH or neutral solution. The reduction reaction equation is as follows:

$$Cr_2O_7^{2-}(aq.) + 14H^+ + 6e^- \rightarrow 2Cr^{3+}(aq.) + 7H_2O \quad (12)$$

So the removal of Cr(VI) is significantly dependent on pH. In addition, the effect of solution pH on the adsorption result is also affected by the surface charge condition of $Ti_3C_2T_x$ solution. The test results of the zeta potential as shown in Fig. 8(b)

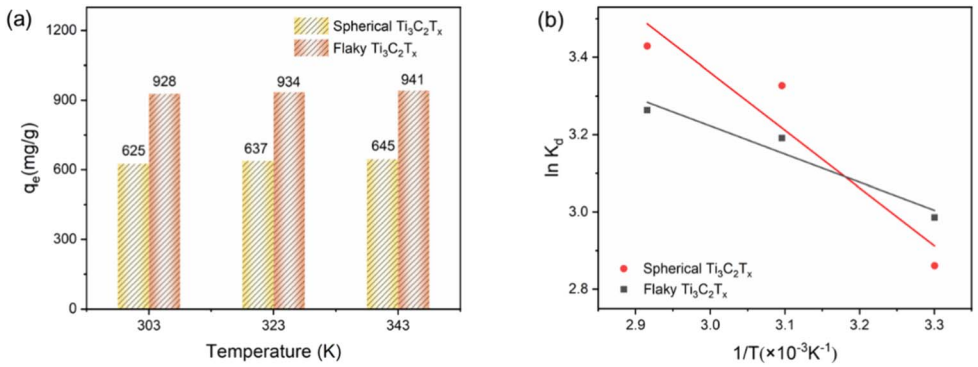

Fig. 7 (a) Graph of adsorption capacity of spherical $Ti_3C_2T_x$ and flaky $Ti_3C_2T_x$ with temperature; (b) van der Waals equation fitting graphs of spherical $Ti_3C_2T_x$ and flaky $Ti_3C_2T_x$ at different temperatures.

Table 3 Thermodynamic parameters of Cr(VI) adsorption by spherical and flaky $Ti_3C_2T_x$

	ΔH (kJ mol^{-1})	ΔS (J mol^{-1} K^{-1})	ΔG (kJ mol^{-1})		
			298 K	308 K	318 K
S–$Ti_3C_2T_x$	12.42	64.85	−6.91	−7.55	−8.20
F–$Ti_3C_2T_x$	6.05	44.90	−7.33	−7.78	−8.22

can well explain the pH dependent adsorption behavior. The point of zero charge (PZC) of spherical and flaky $Ti_3C_2T_x$ solution exists at pH_{PZC} = 2.49 and pH_{PZC} = 2.66, respectively. In solutions with pH less than pH_{PZC}, the more positively charge on the adsorbent surface of $Ti_3C_2T_x$ solution, the greater the electrostatic attraction of the positive charge on the surface of the adsorbent to the electronegative $Cr_2O_7^{2-}$ in the solution. In solutions with pH greater than pH_{PZC}, as the more negative charge on the surface of the adsorbent of $Ti_3C_2T_x$ solution, the electrostatic repulsion of the negative surface of the adsorbent on the negative $Cr_2O_7^{2-}$ in the solution will become greater, resulting in a decrease in adsorption performance. The variation trend of zeta potential is consistent with that of adsorption properties at different pH.

3.7 Adsorption mechanism

In order to further investigate the adsorption mechanism, the binding energy of Cr, Ti and C elements was tested by XPS to investigate the chemical bond changes before and after the flaky $Ti_3C_2T_x$ adsorbed Cr(VI). As shown in Fig. 9(a), the full-spectrum scanning results revealed that peaks of Ti, C, O and F existed in flaky $Ti_3C_2T_x$ before adsorption, and peaks of Cr 2p appeared in $Ti_3C_2T_x$ after adsorption.[39] Fig. 9(b) shows the high-resolution XPS spectra of Cr 2p before and after adsorption. Cr 2p in potassium bichromate before adsorption is composed of Cr(VI) $2p_{1/2}$ (588.6 eV) and Cr(VI) $2p_{3/2}$ (579.4 eV).[40] Cr 2p in $Ti_3C_2T_x$ after adsorption is composed of Cr(III) $2p_{1/2}$ (587.2 eV) and Cr(III) $2p_{3/2}$ (577.6 eV). After adsorption, Cr(VI) was completely reduced to Cr(III).[41] The high-resolution XPS spectra of Ti 2p before and after adsorption is given in Fig. 9(c). It is evident that, prior to adsorption, the Ti 2p consists of $2p_{1/2}$ (459.9, 460.0, 461.9 eV) attributed to C–Ti–T_x, $2p_{3/2}$ (458.2 eV) attributed to Ti–O, $2p_{3/2}$ (454.1, 455.1, 456.3 eV) attributed to C–Ti–T_x. After adsorption, 2p (458.6 eV) and $2p_{3/2}$ (464.6 eV) peaks of Ti–O are added to Ti $2p_{1/2}$, which proves that Ti is oxidized to TiO_2 during the adsorption process. Fig. 9(d) shows the high-resolution XPS spectra of C 1s before and after adsorption.[42] It can be seen that before adsorption, C 1s consisted of C–C (284.8

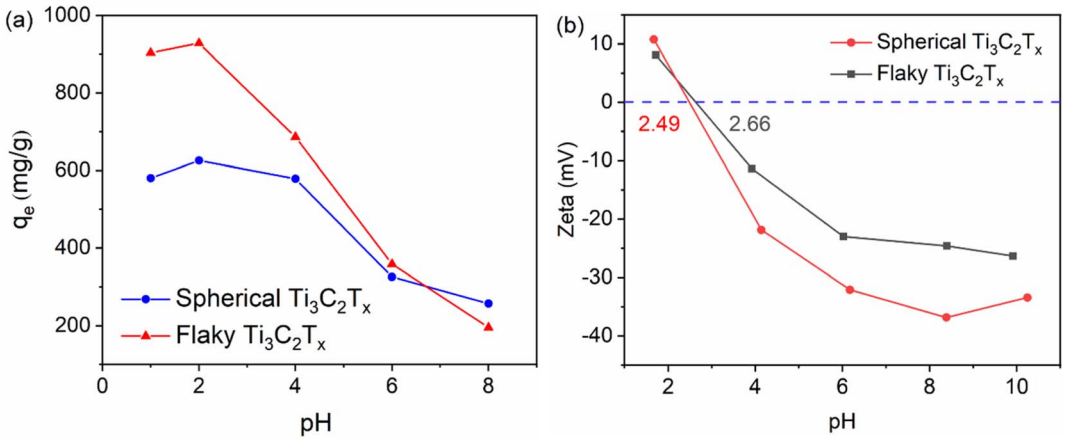

Fig. 8 (a) Maximum adsorption of Cr(VI) by spherical and flaky $Ti_3C_2T_x$ at pH 1, 2, 4, 6, 8 (b) zeta potentials of spherical and flaky $Ti_3C_2T_x$ at different pH.

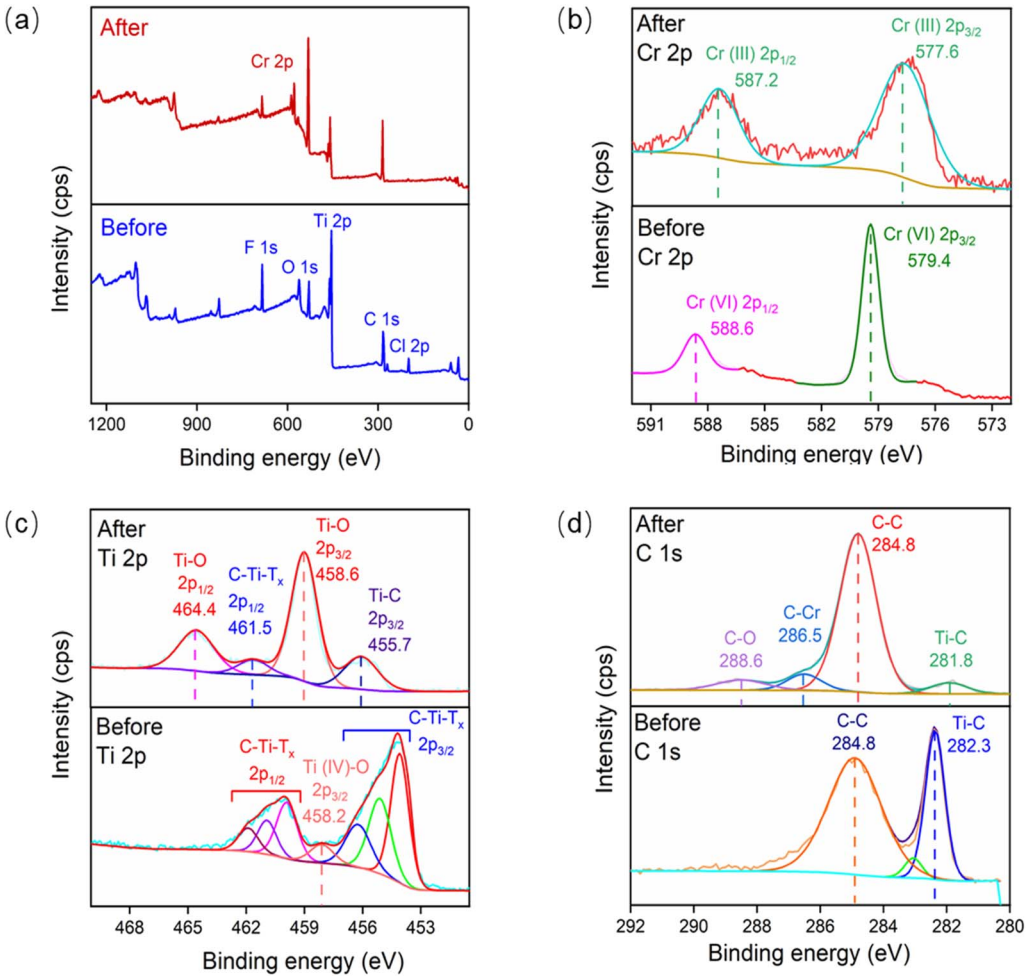

Fig. 9 Comparison of XPS spectra of $Ti_3C_2T_x$ before and after adsorption: (a) full spectrum, (b) Cr 2p, (c) Ti 2p, (d) C 1s.

eV) and Ti–C (282.3 eV), and after adsorption, in addition to the two existing peaks of C 1s, new peaks C–O (288.6 eV) and C–Cr (286.5 eV) appeared, indicating that the C and Cr complexation reaction of $Ti_3C_2T_x$ occurred during the adsorption process (Fig. 10).

The adsorption of Cr(VI) by $Ti_3C_2T_x$ can be divided into three stages. In the first stage, Cr(VI) exists in the form of $Cr_2O_7^{2-}$ before adsorption. In the second stage, the acid is added to the potassium dichromate solution, under acidic conditions, $Cr_2O_7^{2-}$ and H^+ quickly form $HCrO_4^-$ with strong oxidation,[43] and the positively charged $Ti_3C_2T_x$ is easy to adsorb the negatively charged $HCrO_4^-$.[44] On the one hand, due to electrostatic attraction, a small amount of $HCrO_4^-$ physically adsorbs with the O or F terminal on Ti_3C_2. On the other hand, due to the reducibility of $Ti_3C_2T_x$, most $HCrO_4^-$ will be rapidly reduced to Cr(III) by $Ti_3C_2T_x$. In the third stage, part of Cr(III) forms a Ti–O–

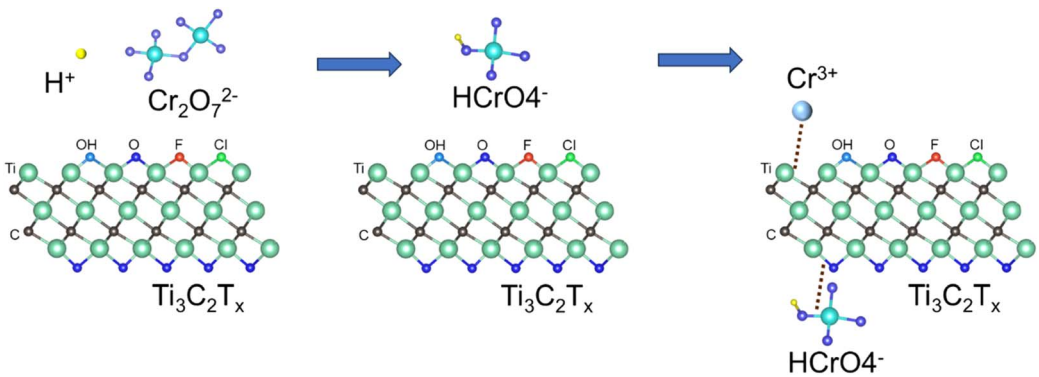

Fig. 10 Schematic diagram of adsorption mechanism of Cr(VI) on $Ti_3C_2T_x$.

Table 4 Comparison of adsorption properties between this work and existing reports on Mxene adsorption of Cr(VI)

Adsorbent	Initial Cr(VI) concentration (mg L^{-1})	Equilibrium time (min)	Maximum adsorption (mg g^{-1})	References
$Ti_3C_2T_x$ powder	400	480	250	45
Multi-layer $Ti_3C_2T_x$	100	720	80	20
ZVI-Alk-$Ti_3C_2T_x$	100	360	198	21
$Ti_3C_2T_x$/Pdmm	100	240	540	46
1CTAB-Ti_3C_2	200	360	206	47
Ti_3C_2@IMIZ	30	80	184	48
Ti_3C_2/TiO_2	50	240	516	49
Spherical $Ti_3C_2T_x$	250	50	626	This work
Flaky $Ti_3C_2T_x$	300	20	928	This work

Cr bond with the O terminal, which is anchored to the surface of $Ti_3C_2T_x$.

The MAC of $Ti_3C_2T_x$ solution for Cr(VI) was compared with the previous reports related to MXene-based absorbent, and the results are listed in Table 4. It can be found that $Ti_3C_2T_x$ sample obtained by spray freezing treatment in this work has a very high adsorption capacity and the fastest adsorption rate, the adsorption properties and equilibrium time of the flaky $Ti_3C_2T_x$ are found to be better than that of the spherical $Ti_3C_2T_x$.

4. Conclusion

In this work, spherical and flaky $Ti_3C_2T_x$ were successfully prepared using spray freezing method. BET analysis shows that the specific surface areas of spherical $Ti_3C_2T_x$ and flake $Ti_3C_2T_x$ are 17.07 $m^2 g^{-1}$ and 17.81 $m^2 g^{-1}$, respectively, which are 1.81 and 1.94 times larger than that of few-layer $Ti_3C_2T_x$. The optimized spherical and flaky structures effectively mitigate the stacking issue of $Ti_3C_2T_x$, thereby providing more adsorption sites. Under the condition of pH 2, the MAC of 20 mg spherical and flaky $Ti_3C_2T_x$ for 100 mL, 250 mg L^{-1} Cr(VI) solution are 626 and 928 mg g^{-1}, respectively. Compared to the few-layer $Ti_3C_2T_x$, MAC increased by 33% and 97%, respectively. The adsorption process of spherical and flaky $Ti_3C_2T_x$ is controlled by chemical adsorption and monolayer adsorption. Thermodynamic experiments have shown that the adsorption reaction is endothermic. By comparing the XPS results before and after adsorption, the adsorption mechanism was discussed in depth. During the adsorption process, unsaturated Ti(II) was oxidized, while Cr(VI) was reduced to Cr(III), indicating that the adsorption of Cr(VI) onto $Ti_3C_2T_x$ is primarily reductive adsorption. In brief, by optimizing the structure of two-dimensional $Ti_3C_2T_x$, the stacking issue of $Ti_3C_2T_x$ was effectively alleviated, and the adsorption capacity was significantly improved in this study. Moreover, the exceptional adsorption capacity and rapid adsorption rate of the flaky $Ti_3C_2T_x$ adsorbent for Cr(VI) make it a promising candidate for practical applications in emergency treatment of Cr(VI) wastewater.

Data availability

The data that support the findings of this study are available on request from the corresponding author.

Conflicts of interest

There are no conflicts to declare.

Acknowledgements

This study was funded by various sources, including the National Natural Science Foundation of China (grant NSFC U22A2078), the Fundamental Research Fund for Central Universities (Project 2022CDJQY-007), the Chongqing Natural Science Foundation (Grant CSTB2022NSCQ-LZX0032), the Open Project of Sichuan Material Corrosion and Protection Key Laboratory (No. 2022CL25), the Sharing Fund of Large-scale Equipment of Chongqing University (202303150164, 202303150169, 202303150178), NHC Key Laboratory of Nuclear Technology Medical Transformation (Mianyang Central Hospital) (No. 2021HYX007), Fundamental Science on Nuclear Wastes and Environmental Safety Laboratory (21kfhk04, 18kfhk02, 20kfhk02). We also thank the Analytical and Testing Center at Chongqing University for conducting XRD, FT-IR, and SEM tests.

References

1 H. Karimi-Maleh, A. Ayati, S. Ghanbari, Y. Orooji, B. Tanhaei, F. Karimi, M. Alizadeh, J. Rouhi, L. Fu and M. Sillanpää, *J. Mol. Liq.*, 2021, **329**, 115062.
2 W. Liu, J. Ni and X. Yin, *Water Res.*, 2014, **53**, 12–25.
3 L. Wei, Q. Li, H. Li, H. Ye, D. Han, Z. Guo and S. Lek, *Ecotoxicol. Environ. Saf.*, 2022, **241**, 113744.
4 H. Wang, F. Wu, Z. Wang, Y. Wang, S. Zhang, H. Luo, Z. Zheng and L. Fang, *Chemosphere*, 2022, **308**, 136573.
5 S. Mahiout, M. Kiilunen, T. Vermeire, S. Viegas, M. Woutersen and T. Santonen, *Regul. Toxicol. Pharmacol.*, 2022, **136**, 105276.
6 G. Asgari, A. Sidmohammadi, A. R. Rahmani, M. R. Samargandi and H. Faraji, *Optik*, 2020, **218**, 164983.
7 L. Ma, N. Chen, C. Feng, Y. Yao, S. Wang, G. Wang, Y. Su and Y. Zhang, *Water Res.*, 2022, **212**, 118144.
8 R. Verma and S. Sarkar, *Ind. Eng. Chem. Res.*, 2020, **59**, 21187–21195.
9 H. Chen, Y. J. Zhang, P. Y. He, C. J. Li and H. Li, *Appl. Surf. Sci.*, 2020, **515**, 146024.

10 P. Basnet, P. K. Ojha, D. Gyawali, K. N. Ghimire and H. Paudyal, *Heliyon*, 2022, **8**, e10305.
11 G. Wang, Y. Hua, X. Su, S. Komarneni, S. Ma and Y. Wang, *Appl. Clay Sci.*, 2016, **124–125**, 111–118.
12 M. Deng, J. Guo, X. Ma, Y. Fu, H. Du, D. Hao and Q. Wang, *Sep. Purif. Technol.*, 2023, **326**, 124786.
13 M. A. Diab, N. F. Attia, A. S. Attia and M. F. El-Shahat, *Synth. Met.*, 2020, **265**, 116411.
14 W. Yao, T. Ni, S. Chen, H. Li and Y. Lu, *Compos. Sci. Technol.*, 2014, **99**, 15–22.
15 K. Eskandari and B. Karami, *Monatsh. Chem.*, 2016, **147**, 2119–2126.
16 M. Helmi, F. Moazami, A. Hemmati and A. Ghaemi, *J. Phys. Chem. Solids*, 2023, **178**, 111338.
17 K. Chu, F. Liu, J. Zhu, H. Fu, H. Zhu, Y. Zhu, Y. Zhang, F. Lai and T. Liu, *Adv. Energy Mater.*, 2021, **11**, 2003799.
18 M. Naguib, M. Kurtoglu, V. Presser, J. Lu, J. Niu, M. Heon, L. Hultman, Y. Gogotsi and M. W. Barsoum, *Adv. Mater.*, 2011, **23**, 4248–4253.
19 H. Deng, Y. Hui, C. Zhang, Q. Zhou, Q. Li, H. Du, D. Hao, G. Yang and Q. Wang, *Chin. Chem. Lett.*, 2024, **35**, 109078.
20 Y. Tang, C. Yang and W. Que, *J. Adv. Dielectr.*, 2018, **8**, 5.
21 L. He, D. Huang, Z. He, X. Yang, G. Yue, J. Zhu, D. Astruc and P. Zhao, *J. Hazard. Mater.*, 2020, **388**, 121761.
22 L. Zhu, R. Ye, P. Tang and P. Xia, *Aust. J. Chem.*, 2022, **75**, 795–798.
23 Q. Li, C. Ge, J. Ma, S. Gu, H. Yang, Y. Xiong, H. Zhou, H. Du, H. Zhu and Q. Wang, *Sep. Purif. Technol.*, 2024, **342**, 126982.
24 R. Liu, J. Li, M. Li, Q. Zhang, G. Shi, Y. Li, C. Hou and H. Wang, *ACS Appl. Mater. Interfaces*, 2020, **12**, 46446–46454.
25 W. Li, S. Zhang, D. He, M. Cai, C. He and X. Fan, *Tribol. Int.*, 2023, **188**, 108877.
26 S. Zhang, H. Ying, B. Yuan, R. Hu and W.-Q. Han, *Nano–Micro Lett.*, 2020, **12**, 78.
27 K. Mustonen, A. Hussain, C. Hofer, M. R. A. Monazam, R. Mirzayev, K. Elibol, P. Laiho, C. Mangler, H. Jiang, T. Susi, E. I. Kauppinen, J. Kotakoski and J. C. Meyer, *ACS Nano*, 2018, **12**, 8512–8519.
28 J. Yan, C. E. Ren, K. Maleski, C. B. Hatter, B. Anasori, P. Urbankowski, A. Sarycheva and Y. Gogotsi, *Adv. Funct. Mater.*, 2017, **27**, 1701264.
29 M. Zhao, X. Xie, C. E. Ren, T. Makaryan, B. Anasori, G. Wang and Y. Gogotsi, *Adv. Mater.*, 2017, **29**, 1702410.
30 H. Zhang, Z. Dai, Y. Sui, N. Wang, H. Fu, D. Ding, N. Hu, G. Li, Y. Wang and L. Li, *Ind. Eng. Chem. Res.*, 2018, **57**, 17318–17327.
31 X. Nie, X. Hu, C. Liu, X. Xia and F. Dong, *Desalination*, 2021, **516**, 115226.
32 J. Gao, Y. Lu, L. Fang, F. Wu, F. Ling, T. Guan, L. Shi, B. Hu and F. Meng, *Environ. Eng. Sci.*, 2018, **35**, 373–381.
33 T. Guan, L. Fang, Y. Lu, F. Wu, F. Ling, J. Gao, B. Hu, F. Meng and X. Jin, *Colloids Surf., A*, 2017, **529**, 907–915.
34 F. Ling, L. Fang, Y. Lu, J. Gao, F. Wu, M. Zhou and B. Hu, *Microporous Mesoporous Mater.*, 2016, **234**, 230–238.
35 Y. Lu, B. Jiang, L. Fang, F. Ling, J. Gao, F. Wu and X. Zhang, *Chemosphere*, 2016, **152**, 415–422.
36 D. Zhang, L. Liu, Z. Ma, H. Hou, X. Wang and S. Yu, *Colloids Surf., A*, 2024, **692**, 133977.
37 A. Shahzad, K. Rasool, W. Miran, M. Nawaz, J. Jang, K. A. Mahmoud and D. S. Lee, *ACS Sustain. Chem. Eng.*, 2017, **5**, 11481–11488.
38 A. Mullick, S. Moulik and S. Bhattacharjee, *Indian Chem. Eng.*, 2018, **60**, 58–71.
39 Q. Wang, H. Zhou, J. Qian, B. Xue, H. Du, D. Hao, Y. Ji and Q. Li, *J. Mater. Sci. Technol.*, 2024, **190**, 67–75.
40 A. R. Khan, S. M. Husnain, F. Shahzad, S. Mujtaba-ul-Hassan, M. Mehmood, J. Ahmad, M. T. Mehran and S. Rahman, *Dalton Trans.*, 2019, **48**, 11803–11812.
41 A. Shahzad, K. Rasool, W. Miran, M. Nawaz, J. Jang, K. A. Mahmoud and D. S. Lee, *ACS Sustain. Chem. Eng.*, 2017, **5**, 11481–11488.
42 X. Xie, C. Chen, N. Zhang, Z.-R. Tang, J. Jiang and Y.-J. Xu, *Nat. Sustain.*, 2019, **2**, 856–862.
43 Q. Wang, W. Ma, J. Qian, N. Li, C. Zhang, M. Deng and H. Du, *Environ. Pollut.*, 2024, **347**, 123707.
44 X. Ma, H. Du, M. Tan, J. Qian, M. Deng, D. Hao, Q. Wang and H. Zhu, *Sep. Purif. Technol.*, 2024, **339**, 126644.
45 Y. Ying, Y. Liu, X. Wang, Y. Mao, W. Cao, P. Hu and X. Peng, *ACS Appl. Mater. Interfaces*, 2015, **7**, 1795–1803.
46 L. Jin, L. Chai, W. Yang, H. Wang and L. Zhang, *Int. J. Environ. Res. Public Health*, 2019, **17**, 167.
47 X. Huang, W. Mu and C. Chang, *J. Alloys Compd.*, 2023, **968**, 172012.
48 G. Yang, X. Hu, J. Liang, Q. Huang, J. Dou, J. Tian, F. Deng, M. Liu, X. Zhang and Y. Wei, *J. Hazard. Mater.*, 2021, **419**, 126220.
49 H. Wang, H. Cui, X. Song, R. Xu, N. Wei, J. Tian and H. Niu, *J. Colloid Interface Sci.*, 2020, **561**, 46–57.